Spatio-temporal reconstruction of avulsion history at the terminus of a modern dryland river system

Donselaar, M.E.; Cuevas Gozalo, M.C.; van Toorenenburg, K.A.; Wallinga, J.

DOI
10.1002/esp.5311

Publication date
2022

Document Version
Final published version

Published in
Earth Surface Processes and Landforms

Citation (APA)
Donselaar, M. E., Cuevas Gozalo, M. C., van Toorenenburg, K. A., & Wallinga, J. (2022). Spatio-temporal reconstruction of avulsion history at the terminus of a modern dryland river system. *Earth Surface Processes and Landforms*, *47*(5), 1212-1228. https://doi.org/10.1002/esp.5311

Received: 13 May 2021 | Revised: 9 December 2021 | Accepted: 11 December 2021

DOI: 10.1002/esp.5311

RESEARCH ARTICLE

ESPL WILEY

Spatio-temporal reconstruction of avulsion history at the terminus of a modern dryland river system

Marinus E. Donselaar[1,2] | Margarita C. Cuevas Gozalo[3] | Koen A. van Toorenenburg[1,4] | Jakob Wallinga[5]

[1]Department of Geoscience and Engineering, Delft University of Technology, Delft, The Netherlands

[2]Department of Earth and Environmental Sciences, KU Leuven, Leuven-Heverlee, Belgium

[3]Independent Researcher, Utrecht, The Netherlands

[4]Shell International Exploration & Production B.V, The Hague, The Netherlands

[5]Netherlands Centre for Luminescence dating & Soil Geography and Landscape Group, Wageningen University, Wageningen, The Netherlands

Correspondence
Marinus E. Donselaar, Department of Geoscience and Engineering, Delft University of Technology, PO Box 5048, 2600 Delft, The Netherlands.
Email: m.e.donselaar@tudelft.nl

Abstract

Fluvial depositional architecture in an unconfined environment is governed by sediment dispersal across the alluvial plain through river-path switching by avulsion. Documented inter-avulsion periodicity from modern rivers ranges from tens to over a thousand years. In this study, a quantitative spatio-temporal reconstruction of avulsion history is presented of the non-vegetated and pristine modern Río Colorado dryland river system in the semi-arid Altiplano Basin (Bolivia), based on the integrated analysis of satellite imagery and absolute age dating using optically stimulated luminescence, complemented with sedimentological and geomorphological ground-truth data. This approach enables us to reconstruct the chronological order of channel belts of the Río Colorado, to determine avulsion recurrence time and inter-avulsion periodicity, to identify mechanisms for flow path changes, and to present a morphodynamic model for the spatio-temporal evolution of fluvial deposits in a semi-arid environment. In a maximum timespan of 12.71 ± 1.5 ka, successive avulsions of the Río Colorado created a sheet of interconnected fluvial deposits, consisting of diverging and juxtaposed alluvial ridges that formed by sediment aggradation in point bars, crevasse splays, levees, and on the channel floor. The ridges show lateral onlap and amalgamation as the result of repeated avulsion and compensational stacking, whereby the river avoided the positive alluvial-ridge relief of its precursors. The resultant morphology is fan-shaped, convex-up with a surface area of approximately 500 km^2 and a maximum observed thickness of 3 m. The results show inter-avulsion periods of the river of up to 1.28 ± 0.34 ka. A paucity in fluvial activity around 2 ka BP, and at present, is interpreted as the result of low river discharge related to long-term dry periodicity in the El Niño Southern Oscillation circulation system. Each river path started as a low sinuous, single-thread channel in a narrow belt, and in time increased its width and sinuosity by point-bar expansion and rotation.

KEYWORDS
alluvial ridges, avulsion frequency, compensational stacking, crevasse splays, endorheic basin, fluvial geomorphology, meandering-channel belts, OSL age determination, river avulsion, semi-arid climate

1 | INTRODUCTION

In an unconfined fluvial environment, river avulsions are the fundamental drivers for sediment dispersal across the alluvial plain (Hajek & Edmonds, 2014; Heller & Paola, 1996; Jones & Schumm, 1999; Leeder, 1978; Mohrig et al., 2000; Slingerland & Smith, 2004), and the formation of an aggradational succession of channel and overbank deposits (Hajek & Wolinsky, 2012; Mohrig et al., 2000; van

Toorenenburg et al., 2018). Avulsions are controlled by the interplay of autogenic processes such as river hydrodynamics, sediment composition and supply rates, floodplain morphodynamics, breaching of river levees, alluvial-ridge aggradation, differential compaction of mud-prone floodplain with respect to sand-prone alluvial-ridge sediment, and related changes in along-river and cross-valley gradient (Aslan et al., 2005; Edmonds et al., 2016; Hajek & Edmonds, 2014; Hajek & Wolinsky, 2012; Jones & Schumm, 1999; Mohrig et al., 2000; Nicholas et al., 2018; Slingerland & Smith, 1998; van Toorenenburg et al., 2018). He et al. (2020), Stouthamer and Berendsen (2007), and Timár et al. (2005) documented allogenic processes (sea-level change, tectonics) as a cause of river avulsion. Berendsen and Stouthamer (2000) and Cohen et al. (2005) documented differential subsidence across Roer Valley Graben faults in the North Sea Basin as an independent local control on the occurrence of avulsions in the Rhine–Meuse Delta. Slingerland and Smith (2004) presented a comprehensive review of the different types of avulsion based on Holocene and modern examples, one of which, termed 'progradational avulsion', is a response to alluvial-ridge aggradation and associated decrease in channel gradient and flow efficiency (Hajek & Wolinsky, 2012; Kleinhans et al., 2013; Slingerland & Smith, 2004; Törnqvist & Bridge, 2002). Alluvial ridges aggrade through deposition in levees and crevasse splays, and associated accumulation of channel-floor sediment, super-elevating the river thalweg relative to the surrounding floodplain surface until the river avulses to a hydrodynamically more favourable, steeper path (Ethridge et al., 1999; Hajek & Wolinsky, 2012; van Toorenenburg et al., 2016, 2018). Mohrig et al. (2000) found that this process of avulsion occurs at a normalized super-elevation (i.e. the ratio between levee height above the floodplain divided by channel depth) of 1.0 ± 0.5. From a flume-experiment study of channel avulsion in a backwater-controlled deltaic setting, Ganti et al. (2016) concluded that in-channel sedimentation, rather than super-elevation, was the prime control on the occurrence of river avulsion, with a depositional depth of 0.3 ± 0.13 of the total channel depth as avulsion threshold.

Avulsions have been documented from modern rivers such as the Kosi River in India (Chakraborty et al., 2010; Sinha, 1996, 2009; Wells & Dorr, 1987), Brahmaputra River in Bangladesh (Bristow et al., 1999), Rhine–Meuse Delta in the Netherlands (Stouthamer & Berendsen, 2001), Saskatchewan River in Canada (Slingerland & Smith, 2004; Smith et al., 1989), Yellow River in China (Ganti et al., 2014; Slingerland & Smith, 2004), and Tshwane River in South Africa (Larkin et al., 2017). Valenza et al. (2020) documented downstream changes in avulsion style in various remotely sensed modern rivers, from reoccupation of abandoned braided channels in the upstream part of the river trajectory, to flooding and sedimentation during avulsion-channel formation in the downstream meandering river part. Documented avulsion frequencies range from once every 0.028 ka (Kosi River; Slingerland & Smith, 2004) to four occurrences in 5 ka (Mississippi River; Aslan et al., 2005). Studies of preserved avulsion deposits in the rock record are few (e.g. Berendsen & Stouthamer, 2000; Coronel et al., 2020; Flood & Hampson, 2014; Jones & Hajek, 2007; Kraus & Wells, 1999; van Toorenenburg et al., 2016) and yield limited information on the mechanisms and frequency of avulsion. The cause of this shortcoming may be that: (1) avulsion frequencies in the rock record are expected to be beyond the resolution of existing geochronological methods, given the short avulsion recurrence time interpreted from modern settings; and (2) the lack of reliable correlation surfaces hampers the interpretation and quantification of river gradient, floodplain aggradation, super-elevation, or avulsion geochronology. Palaeosols have been proposed as correlation surfaces in the rock record (Hajek & Wolinsky, 2012; Kraus & Wells, 1999). The analysis of the chronological order of river avulsions from the stratigraphical position of channel deposits depends on the assumption that palaeosols formed on a topographically flat and horizontal floodplain surface, and that post-depositional differential compaction has not altered the original geomorphology. These uncertainties may impair the use of palaeosols as a reference surface for quantification of avulsion parameters in the rock record.

In this study, we aim to: (a) quantitatively reconstruct the order, chronology, and recurrence time of avulsions of the Río Colorado over the last ~12 ka; (b) discuss the mechanisms for the flow-path changes; and (c) present a morphodynamic model for the spatio-temporal evolution that captures the organization of aggrading fluvial deposits in a semi-arid environment. To this end, we integrate remote-sensing-based mapping of the modern Río Colorado dryland river system in the semi-arid Altiplano Basin (Bolivia) with absolute age dating of fluvial sediment samples using optically stimulated luminescence (OSL), and with sedimentological and geomorphological ground-truth observations and high-resolution differential-GPS (dGPS) surveys. The results of this study will broaden our understanding of fluvial morphodynamics and sediment transport processes in a pre-vegetation earth (cf. Ganti et al., 2019; Ielpi, 2019; Ielpi & Lapôtre, 2019, 2020; Ielpi, Fralick, et al., 2018; Ielpi, Ghinassi, et al., 2018), and in the context of climate-change-related aridification of alluvial basins.

2 | STUDY AREA

The study area is located in the southeast part of the endorheic Altiplano Basin (Bolivia), which is a high-altitude hinterland plateau (3650–4200 m above mean sea level) enclosed by the Eastern and Western Andean Cordilleras (Figure 1; Horton et al., 2001). The basin fill consists of Cretaceous to Holocene alluvial and lacustrine sediments (Elger et al., 2005). Alternating wetter and drier climate periods during the Pleistocene and Holocene resulted in short-duration, high-amplitude base-level fluctuations in the basin (Baker et al., 2001; Chepstow-Lusty et al., 2005; Fornari et al., 2001; Placzek et al., 2006; Rigsby et al., 2005; Servant et al., 1995; Sylvestre et al., 1999). The fluvial deposits of the Río Colorado dryland river system accumulated after the last base-level highstand of 13.4–11.5 ka (Baker et al., 2001) when the Coipasa Palaeolake was up to 55 m above the present-day base level (Bills et al., 1994; Placzek et al., 2006). The total area of fluvial sedimentation is approximately 500 km^2 and attains a maximum observed thickness of 3 m (Donselaar et al., 2013). The river gradient is extremely low (averaging 8.3×10^{-5}) with an along-channel drop in thalweg elevation of 3 m over 36 km. At present, the basin is in a dry-climate period with an average annual precipitation of 0.20 m/a (Argollo & Mourguiart, 2000) and an evapotranspiration potential of 1.5 m/a (Grosjean, 1994; Risacher & Fritz, 2009). As a consequence, lakes on the southern part of the plateau are ephemeral or have dried up, and river systems such as the Río Colorado now terminate on the alluvial plain bordering the present-day salt lake

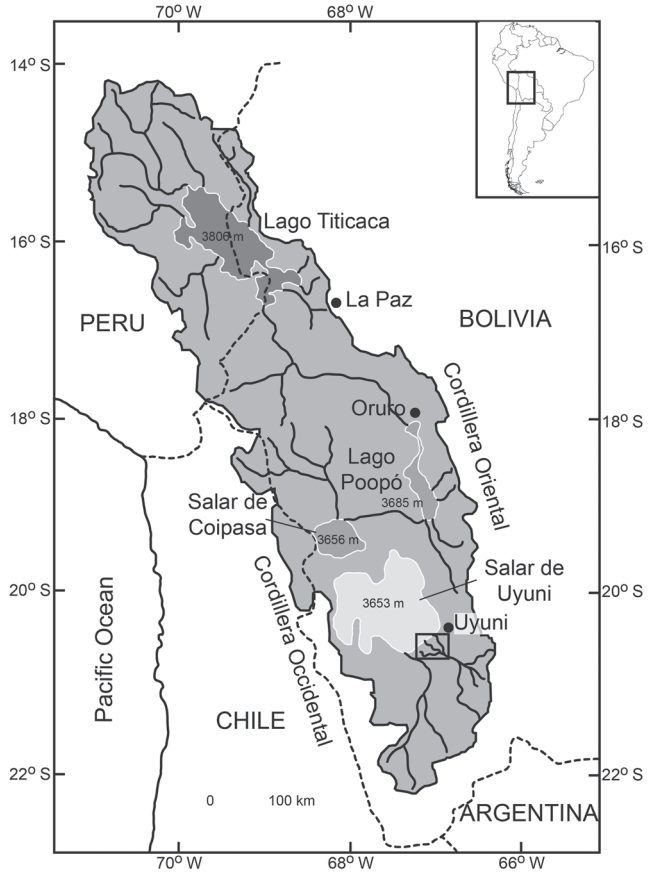

FIGURE 1 The endorheic Altiplano Basin with the Salar de Uyuni sub-basin spanning ~12 500 km^2. Box near Uyuni indicates the Río Colorado dryland river system (Figure 2). Modified from Baker et al. (2001), Fornari et al. (2001), and Placzek et al. (2006)

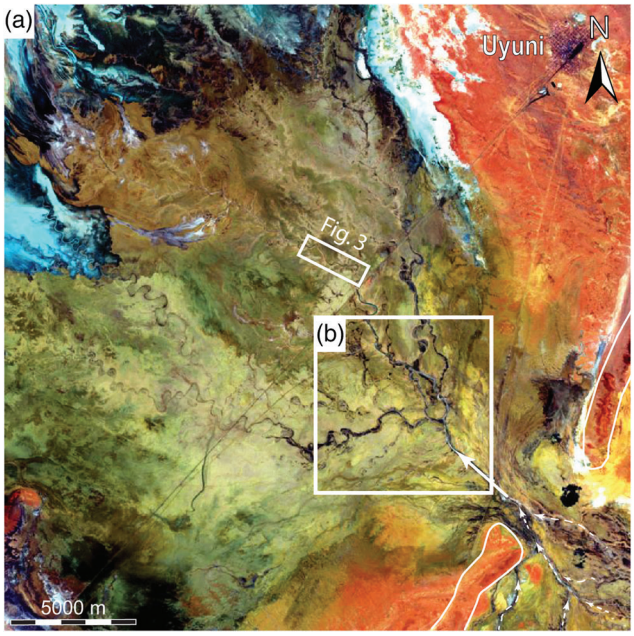

FIGURE 2 (a) Landsat-7 ETM + image (band combination 5, 3, 1) of the Río Colorado terminus (image date 16 November 2002). Flow is to the northwest. Note the downstream change of river morphology from a tributary pattern (dashed arrows in the lower-right corner) to the straight midstream part (solid arrow) to divergent pattern of avulsed river paths. The white-blue-brownish colours in the upper-left corner correspond to the Salar de Uyuni. Outline of topographically higher area in southeast corner accentuated with solid white lines. (b) Study area (~44 km^2) with avulsion network (see Figure 6)

(Figure 2). The study area is extremely flat, in part due to deflation in the dust storm events of July 2009 and July 2010 (Gaiero et al., 2013), and is a non-vegetated, pristine area, without anthropogenic alteration.

The Río Colorado is an endogenic ephemeral dryland river (cf. Bull & Kirkby, 2002) in a semi-arid climate. Annual rainfall in the study area is less than 0.2 m/a (Argollo & Mourguiart, 2000), and the evapotranspiration potential is 1.5 m/a (Grosjean, 1994; Risacher & Fritz, 2009). The river drains part of the Eastern Cordillera and is characterized by prolonged periods (multiple months up to years) of drought alternating with short (less than 24 h), severe peak-discharge events (Donselaar et al., 2013; Garreaud et al., 2003; Li, 2014; Li et al., 2014). Peak discharge in the study area takes place in the austral summer months (December to March) with short periods of intense rainfall (Donselaar et al., 2013). Transmission losses are high in the dry-climate setting due to flood-outs onto the adjacent floodplain, evapotranspiration, and infiltration in the floodplain surface (Costa et al., 2012, 2013; Jarihani et al., 2015; Knighton & Nanson, 1994; Lange, 2005). In combination with the very low thalweg gradient in the terminal part of the Río Colorado, this results in a downstream decrease of the river width and depth (Donselaar et al., 2013). In peak-discharge periods, the flood water spills out of the channel confinement via multiple levee breaches and forms extensive, laterally amalgamated crevasse-splay lobes fringing the river (Figure 3; Donselaar et al., 2013; Li et al., 2014).

The tributaries of the Río Colorado converge to a straight midstream part that enters the southeast corner of the study area (Figure 2). The distal part of the Río Colorado is characterized by deposition of fine to very fine sand and silt in a background of floodbasin silt and clay. Donselaar et al. (2013) showed that the river system prograded and expanded laterally by multiple avulsions, which resulted in an apparent distributary pattern of successive avulsed meandering-channel belts. Donselaar et al. (2013) provided a preliminary reconstruction of relative ages based on Google Earth-Pro imagery and the principle that younger channel belts truncate older ones.

3 | DATA AND METHODS

The work presented here is a multidisciplinary approach of Google Earth-Pro satellite-imagery analysis, ground-truth fieldwork observations of the fluvial morphology with dGPS surveys and laser rangefinder measurements, analysis of sedimentological data on the surface and in shallow trenches, and laboratory sediment-sample analysis for OSL dating. Fieldwork campaigns were carried out in 2010, 2011, 2014, and 2016 during the Austral spring (September to November) at the end of the dry season when the river was in its low-flow stage and the area was best accessible. All outcrop data points were geo-referenced with handheld GPS devices and dGPS measurements.

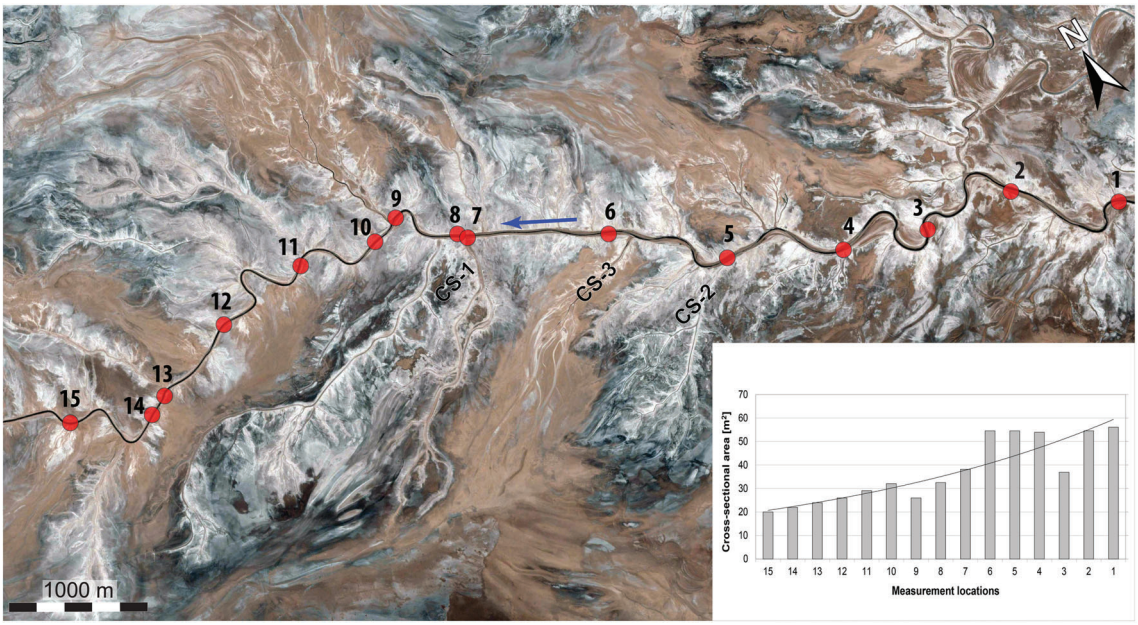

FIGURE 3 Multiple, laterally connected crevasse-splay channel and lobe deposits (light grey) fringe the Río Colorado. Downriver width–depth decrease (W: 28.4 to 15.4 m; D: 1.7 to 1.3 m) over channel-thalweg distance of 9.7 km between measuring stations 1 (20°32′14.58″S, 66°54′30.05″W) and 15 (20°30′46.80″S, 66°58′36.94″W) results in a decrease of channel cross-sectional area of 64% (insert). Blue arrow: Flow direction. Crevasse-splay lobe CS-3 fill postdates the adjacent lobes CS-1 and CS-2 and fills the topographic depression between the two. CS-3 first appearance in Google Earth-Pro imagery is 20 July 2013, expanding ever since

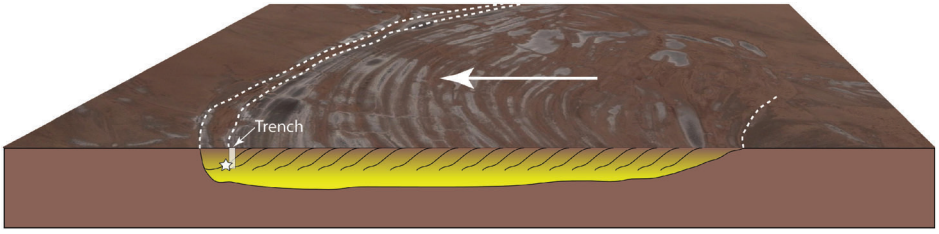

FIGURE 4 Schematic cross-section through a point-bar sequence, showing the direction of point-bar expansion. Samples for OSL dating (star) were taken in 0.6–1.0 m-deep trenches (white rectangle) dug into the last point-bar accretion surface, just below the interface with the abandoned-channel fill, with the aim to capture the time of channel-belt abandonment

The geomorphological expression of channel belts in the study area was captured with field measurements and Google Earth-Pro 2016 satellite imagery, with an improved resolution with respect to the 2004 images used by Donselaar et al. (2013). Laser rangefinders with 20 cm resolution were used to verify crevasse-splay radii and point-bar radii on the ground, and to measure river width and depth (Figure 3). In addition, subtle surface topography—such as the height difference across alluvial ridges and to the adjacent floodplain—was recorded at centimetre-scale resolution in dGPS surveys. The sinuosity index (SI) of channels was established in Google Earth-Pro as the ratio of channel-thalweg length to channel-belt length (cf. Leopold & Wolman, 1957; Schumm, 1963). Satellite imagery and laser rangefinder measurements yielded the channel widths and point-bar radii.

The absolute age of each abandoned channel belt was determined by OSL dating of sediment samples collected in the field. To obtain these, shallow trenches (0.6–1.0 m deep) were dug in the abandoned, filled-in river channels adjacent to the point bars. Seventeen samples were collected at the last lateral-accretion unit of a point bar with the aim to capture the time just prior to channel-belt abandonment (Figure 4). One sample ('Lac') was taken from underlying diatom-rich lacustrine sediment (Figure 5) to validate earlier chronologies for occurrence of a lake. Finally, an additional sample (Figure 6, sample 12) was taken from the first-formed accretion surface associated with the present-day Río Colorado, with the aim to capture the time of initiation of the most recent channel belt. The samples were collected in black PVC or steel tubes and wrapped in black tape to prevent exposure to daylight. OSL measurements and analyses were carried out at the Netherlands Centre for Luminescence dating. Equivalent doses were obtained by measuring OSL signals on small aliquots of sand-sized quartz grains (Murray & Wintle, 2003), and palaeodoses were then derived by applying the bootstrapped minimum age model (BSMAM) to the equivalent dose distribution (Cunningham & Wallinga, 2012) (see online Supplementary Information for details). Sample OSL age was defined as the ratio of palaeodose to dose rate. Note that all time values in this paper are denoted as best estimate ± standard error (68% confidence interval).

The inter-avulsion period (i.e. the absolute time between consecutive avulsions) was estimated as the difference between OSL abandonment ages of consecutive channel belts. These interval times

are presented as a normal difference distribution with its lower tail truncated at zero, given that the relative order of the sampled channel belts is known (hence, the difference cannot be negative). Note that this interval time includes any period of coeval activity (e.g. during gradual avulsion).

The active migration time of each channel belt was estimated as the quotient of maximum point-bar radius over estimated migration rate, based on the empirical power-law correlation between average channel width and migration rate (Ielpi & Lapôtre, 2020):

$$Mr_{(unveg)} = (0.13 \pm 0.02)\, w_{(unveg)}^{(0.84 \pm 0.08)} \quad (1)$$

in which $Mr_{(unveg)}$ is the migration rate of the non-vegetated river (m/y), and $w_{(unveg)}$ the measured river width (m). The power law is derived from satellite-imagery-based time-series analysis of dryland rivers in the Great Basin of North America, the Iranian Plateau of western Central Asia, and the Río Colorado in the Altiplano Basin (see Ielpi & Lapôtre, 2020 and the online Supplementary Information for complete dataset). By definition, the active migration time should not exceed the inter-avulsion period, but it can be less when the channel is not actively migrating throughout the inter-avulsion period (i.e. ephemeral discharge). The active migration time is subsequently expressed as a fraction-% of the inter-avulsion period. Note that post-abandonment migration through reuse of the remnant channel

FIGURE 5 Contact (dashed line) between light-green, diatom-rich lacustrine sandy clay and overlying red-brown very fine-grained fluvial sand. Sample 'Lac' near bottom of the trench at 0.7 m below the surface. Hammer (30 cm) for scale. For location, see Figure 6

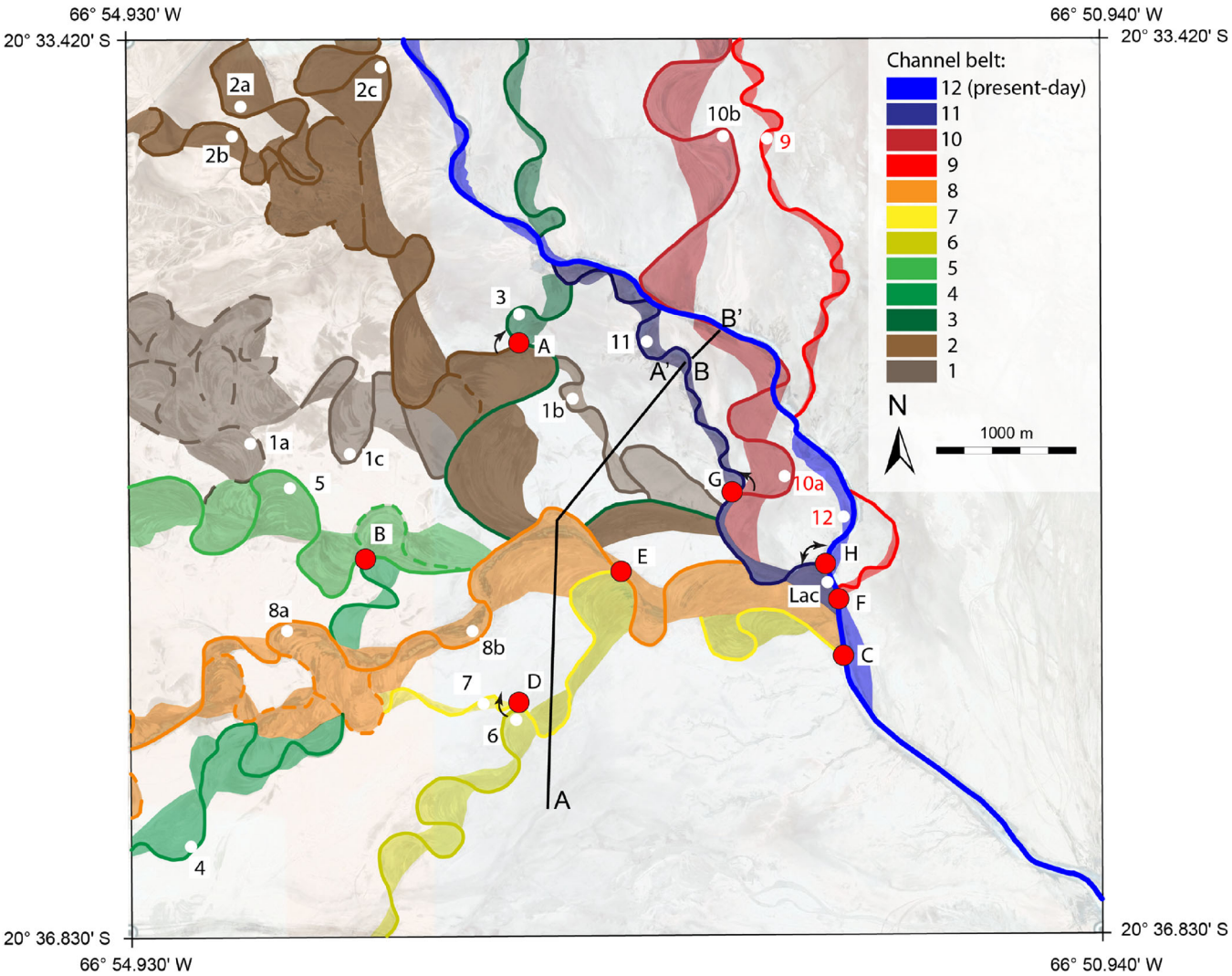

FIGURE 6 Spatio-temporal reconstruction of channel belts in the study area (see Figure 2b for location) with their relative geochronological order indicated by different colours. OSL sample locations indicated by labelled white dots, avulsion points by labelled red dots. Lines A–A′ and B–B′: dGPS profiles in Figure 10

depression (e.g. draining the inundated floodplain) was assumed to be negligible.

4 | RESULTS

4.1 | Fluvial sedimentology and geomorphology

The improved resolution of the Google Earth-Pro imagery allowed for the expansion of the number of different channel belts from 8 (figure 13 in Donselaar et al., 2013) to 12 (Figure 6). The mapped channel belts formed by deposition of fine to very fine sand and silt in point bars, levees, and as channel-floor deposits (Figures 3, 7, and 8). Each of the channel belts defined in this study comprises a single-channel sinuous river with SI ranging from 1.25 for channel 7 to 2.56 for channel 2. Bars in the inner bends of the channels show that lateral accretion of fluvial sediment occurred by expansion of lateral bars in the immature low-sinuosity channels, and by expansion and downstream translation and rotation of point bars in well-developed meandering channels (cf. Brice, 1974; Bridge, 2006; Daniel, 1971; Jackson, 1976). The scroll-bar morphology of the point bars is accentuated by the occurrence of salt evaporates in the coarser-grained ridges (Figures 7 and 8f).

River-path changes are by nodal avulsion, with the exception of river courses 10 and 12, which show an anastomosing morphology with the avulsed channel (cf. Makaske, 2001) as a local avulsion that further downstream reoccupies parts of predecessor channels 9 and 11. Eight nodal avulsion points (A–H in Figure 6) could be reconstructed. The locations of the avulsion from channel belts 1 to 2 and 3 to 4 have been obliterated by posterior river paths.

The abandoned channels have filled in with cross-laminated very fine sand in the lower part, to silt and clay at the top (Figure 8c), except for the last-avulsed river path (Figure 9) and sections of its predecessors north of the modern river, which are only partially infilled and maintain a remnant channel morphology. At the junction of the last-avulsed channel with the present-day river, a sediment threshold has formed at the avulsion location by deposition of ripple-laminated very fine sand (Figures 8d and e). After completion of the channel infill, the river-channel morphology is a flat surface (Figure 8f). In the waning stage of the ephemeral, short-duration (<24 h) peak-discharge events, the peak-water surge moved further downriver and the water level quickly dropped (Figure 8b). Evaporation and infiltration in the surface precluded the development of a permanent standing water body.

Crevasse splays formed along both sides of the river (Figures 7 and 8a). Individual crevasse-splay lobes attain thicknesses up to 25 cm close to their apex, and can reach a radius of >2000 m (Figure 3). Aggradation of levees (defined here as the product of unconfined overbank flow fringing the channel; Figure 8b) and laterally amalgamated and vertically stacked crevasse-splay lobes (Figure 3) created an elevated rim bordering the parent channel. The resulting vertical growth of bankfull height produced an increase of in-channel accommodation, and the potential for channel-floor sediment accumulation (van Toorenenburg et al., 2018). In combination with point-bar expansion by lateral accretion, the process of aggradational sedimentation created an alluvial ridge with a gentle slope towards the surrounding floodplain (Figures 7 and 10).

4.2 | Channel-belt geochronology

The uppermost lacustrine sediments in sample 'Lac' are OSL dated to 12.7 ± 1.5 ka (Table 1, Figures 5 and 11a), which is in accordance with the most recent Coipasa Palaeolake highstand that lasted until 11.5 ka (Baker et al., 2001). This provides a maximum age for the fluvial deposits of the Río Colorado that are directly overlying the lacustrine sediments.

Channel belt 1 is the oldest abandoned river path captured in this study and displays a westward palaeoflow direction (Figure 6). The intermittent exposure of this channel belt is due to partial reworking by posterior river trajectories. Three OSL samples (1a, 1b, and 1c), taken from preserved river sections, returned similar river-

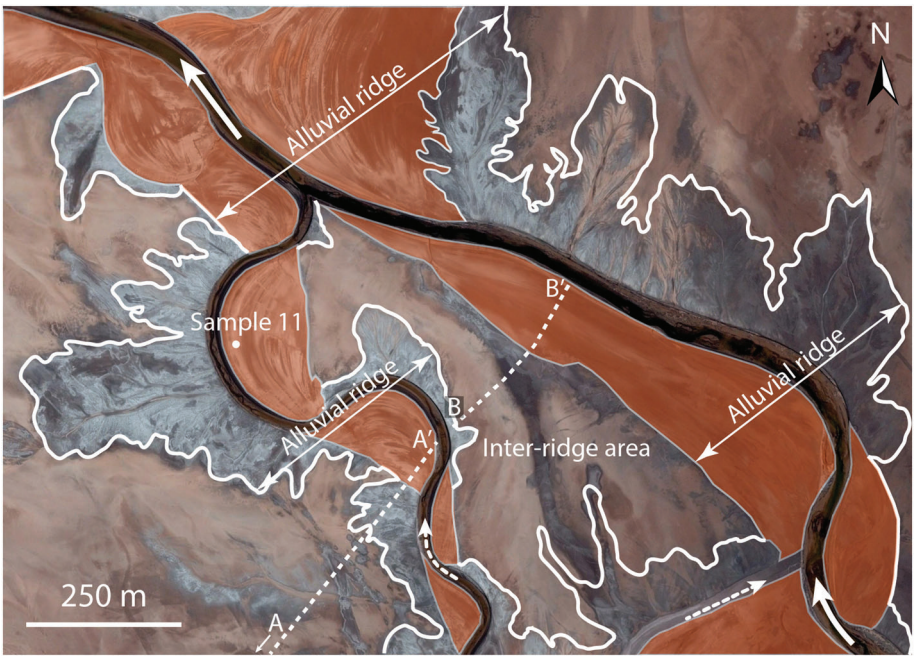

FIGURE 7 Visualization on a Google Earth-Pro image of the formation of alluvial ridges by accumulation of sand in point bars (reddish brown) and crevasse-splay and levee deposits (grey, outlined in white). Flow direction towards the northwest (arrow). Lines A–A′ and B–B′ correspond to the dGPS profiles in Figure 10

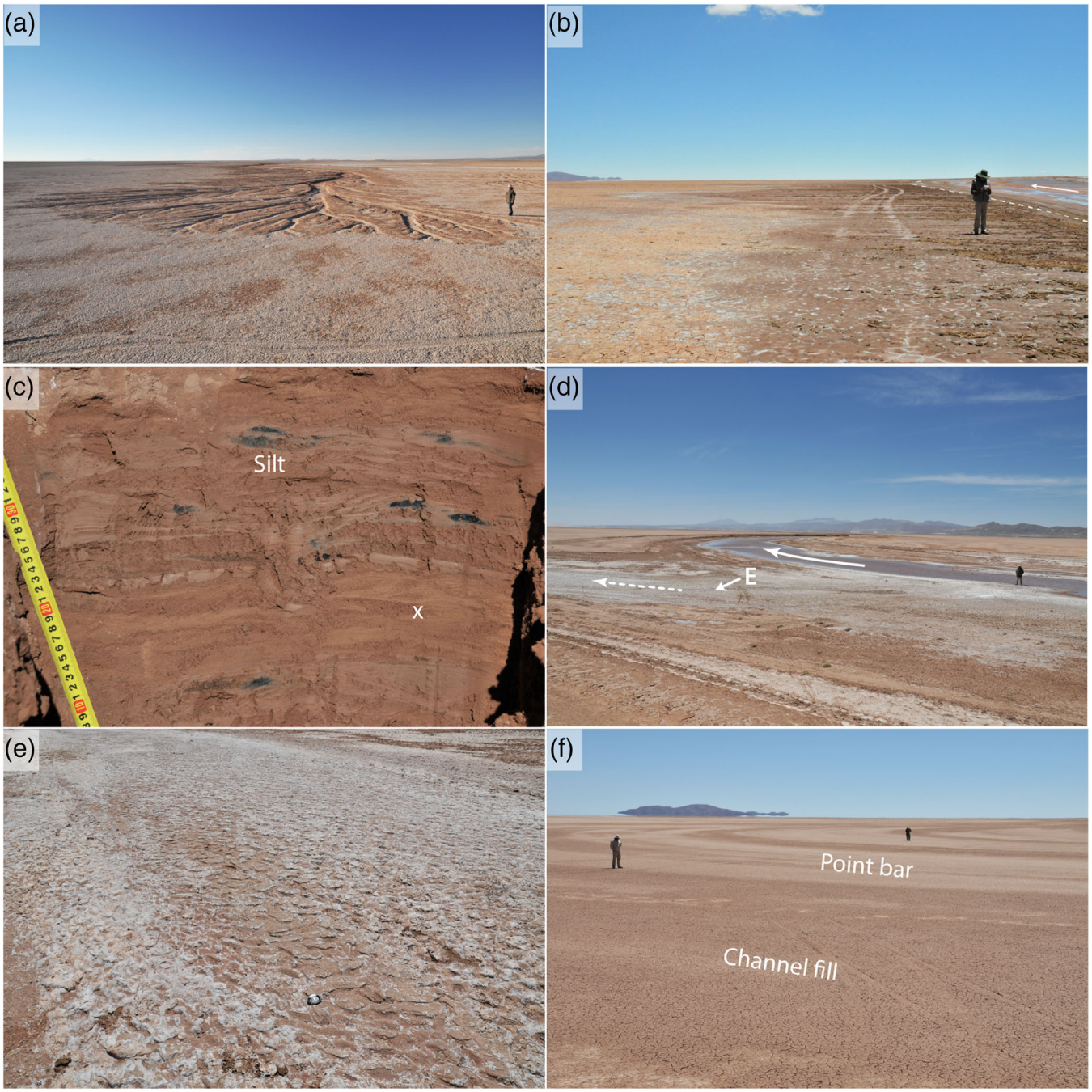

FIGURE 8 (a) Small, lobate crevasse-splay (L = 250 m; W = 50 m; D = 0.20 m) consisting of very fine sand deposits crossed by shallow, branching channels. The splay was emplaced between February 2004 (not yet visible on Google Earth-Pro imagery) and the fieldwork campaign of October 2011. MCG (1.58 m tall) for scale. Location: 200 m east of sample location 11 (Figure 6). (b) Levee deposits (darker colour) of very fine sand and organic debris expands on the adjacent floodplain (lighter colour). Picture taken 24 October 2014, one week after a short peak-discharge event caused a minor flooding of the area. The width of the levee deposits is 10–25 m. Note that the river level had by then already subsided. Arrow: Flow direction; dashed line: Bankfull height. Person (1.75 m tall) for scale. Location: Close to avulsion point C (Figure 6). (c) Channel fill of very fine-grained, ripple-laminated sand (x) silt and clay. Black streaks: Organic debris. Sample location 11 (Figure 6). (d) Avulsion point H (Figure 6) at the split between present-day river path 12 (solid arrow) and last-avulsed channel 11 (dashed arrow). Sedimentation at the entry of the avulsed channel forms a threshold. Location of Figure 8e indicated by 'E'. Person (1.75 m) for scale. (e) Linguoid, very fine-grained sandy ripples at the entry of the avulsed channel. Flow towards the viewer, into the avulsed channel. Lens cap (7 cm) for scale. Location: Figure 8d. (f) Alternating ochre and light grey, salt-cemented curved lines are the surface expression of scroll-bar morphology of the point bar. Channel (foreground) completely filled with very fine sand, silt, and clay. Photo, taken 24 September 2010, witnesses the flat deflation surface after the 18 July 2010 major dust-storm event (Gaiero et al., 2013). Person (left) is 1.75 m tall. Sample location 8a (Figure 6)

abandonment ages, the youngest of which is 3.63 ± 0.29 ka ('Age' in Table 1 and Figure 11a). As the onset of this river path has not been dated, it is not possible to establish a duration of activity for this channel belt.

Channel-belt complex 2 partly truncates channel belt 1 and flowed to the northwest (Figure 6). The relative geochronology of the sampled river paths cannot be established from satellite imagery or dating because of the associated OSL age uncertainties. The youngest

FIGURE 9 Remnant channel depression of last-avulsed channel; view to the northwest. Channel width: 20 m. Location: Sample location 11 (see Figure 6)

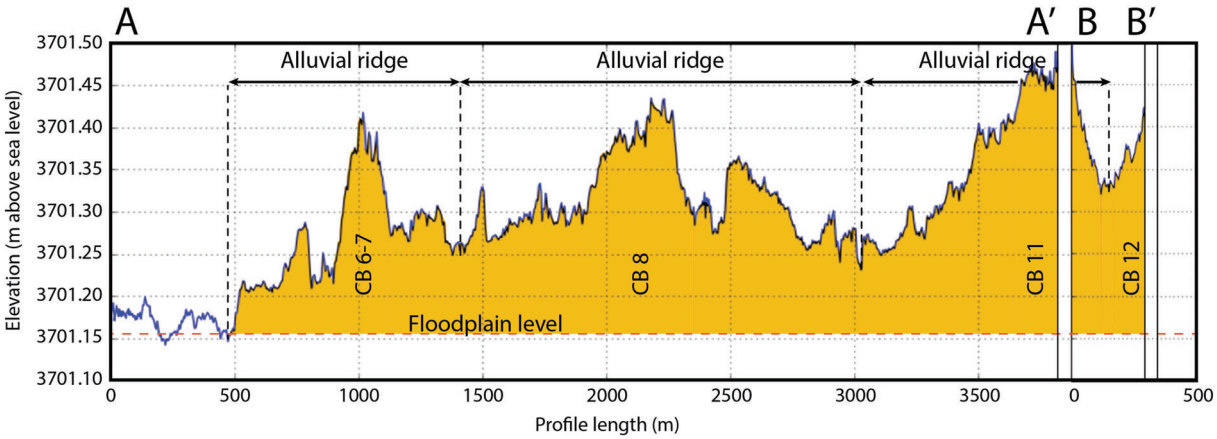

FIGURE 10 dGPS profile across abandoned (CB 6–7, 8, 11) and present (CB 12) channel belts (CBs) with numbers corresponding to Figure 6. Discontinuation between A′ and B indicates the residual channel of the last-avulsed river; discontinuation at B′ is the present-day river

abandonment in the complex of channel belt 2 is dated at 2.35 ± 0.18 ka (Table 1 and Figure 11a), a time difference of 1.28 ± 0.34 ka compared to the latest abandonment age of channel belt 1 (inter-avulsion period in Table 2 and interval time in Figure 11b). This does not necessarily represent the lifespan of the channel-belt 2 complex, as there is no evidence of a direct avulsion from channel belts 1 to 2 (i.e. the avulsion point is not exposed, hence the possibility that one or more unidentified channel belts have been active intermediately cannot be excluded).

Channel belt 3 originated from avulsion point A and shows a palaeoflow direction to the north, bypassing the alluvial-ridge geomorphology of channel belts 1 and 2 (Figure 6). The river path of channel 3 upstream from avulsion point A followed that of channel 2 without truncating or enlarging the point bars of channel belt 2. Downstream from avulsion point A, channel 3 developed a narrow channel belt with SI of 1.58. Sample 3 shows an abandonment age of 2.23 ± 0.17 ka (Table 1 and Figure 11a). The exposure of avulsion point A demonstrates direct succession from channel belt 2. From this, it follows that the inter-avulsion period for channel belt 3 is 0.12 ± 0.25 ka (Table 2 and Figure 11b).

Channel belt 4 shows a palaeoflow direction to the southwest, bypassing previously active river tracts in the northwest quadrant of the study area (Figure 6) and changing to a westerly direction beyond the study area. The avulsion point from which the river path originated is not exposed because of truncation by posterior river paths 5 and 8, hence it is not possible to constrain the onset of this channel belt. The abandonment age captured in sample 4 is 2.24 ± 0.32 ka (Table 1 and Figure 11a). Note that the mean abandonment age is older than that of channel belt 3. The associated 51% left truncation of the inter-avulsion period indicates a high probability of these channel belts having been (partly) coeval.

Channel belt 5 diverted from channel belt 4 at avulsion point B with a palaeoflow direction to the west (Figure 6). Upstream of the avulsion point, the new channel developed its own meanders that eroded the channel deposits of its precursor. The abandonment age in sample 5 is 2.26 ± 0.24 ka (Table 1 and Figure 11a), which yields an inter-avulsion period of 0.02 ± 0.40 ka (Table 2 and Figure 11b). Again, the negative mean and corresponding 52% left truncation are indicative of (partly) concurrent activity.

TABLE 1 OSL dating results (values as best estimate ± standard error). Quality assessment based on assessment of the equivalent dose distribution. Sigmab denotes expected overdispersion for well-bleached samples and differs between samples due to grain size used for analysis and measurement protocol (Cunningham et al., 2011). OD denotes the overdispersion as determined for the sample using the central age model (Galbraith et al., 1999). Unreliable data are in italics. One outlier in sample 10b was removed

Sample	Latitude	Longitude	Lab code	Palaeodose [Gy]	Dose rate [Gy/ka]	Age [ka]	Error (s/r) [ka]	Quality	Notes
Lac	20°35.450′S	66°52.069′W	NCL-5110117	26.90 ± 2.89	2.12 ± 0.10	12.71 ± 1.50	0.44/1.44	+	BSMAM (sigmab 26 ± 7%, OD 22%)
1a	20°34.958′S	66°54.429′W	NCL-5114056	14.17 ± 1.12	3.84 ± 0.19	3.69 ± 0.34	0.12/0.32	+	BSMAM (sigmab 18 ± 3%, OD 34%)
1b	20°34.738′S	66°53.143′W	NCL-5114053	19.71 ± 0.97	5.39 ± 0.22	3.65 ± 0.24	0.12/0.20	+	BSMAM (sigmab 18 ± 3%, OD 2%)
1c	20°34.947′S	66°54.057′W	NCL-5114049	14.89 ± 0.92	4.10 ± 0.22	3.63 ± 0.29	0.12/0.27	++	BSMAM (sigmab 18 ± 3%, OD 13%)
2a	20°33.695′S	66°54.503′W	NCL-5114051	11.19 ± 0.92	4.06 ± 0.16	2.76 ± 0.25	0.09/0.24	++	BSMAM (sigmab 18 ± 3%, OD 17%)
2b	20°33.763′S	66°54.512′W	NCL-5114052	10.62 ± 0.58	4.27 ± 0.20	2.49 ± 0.18	0.08/0.16	++	BSMAM (sigmab 18 ± 3%, OD 12%)
2c	20°33.557′S	66°53.882′W	NCL-5114050	8.02 ± 0.48	3.41 ± 0.15	2.35 ± 0.18	0.11/0.14	++	BSMAM (sigmab 18 ± 3%, OD 14%)
3	20°34.508′S	66°53.326′W	NCL-5112110	7.64 ± 0.48	3.43 ± 0.16	2.23 ± 0.17	0.08/0.15	+	BSMAM (sigmab 26 ± 7%, OD 20%)
4	20°36.531′S	66°54.709′W	NCL-5114057	7.86 ± 1.06	3.51 ± 0.17	2.24 ± 0.32	0.07/0.31	+	BSMAM (sigmab 18 ± 3%, OD 22%)
5	20°35.095′S	66°54.314′W	NCL-5112111	7.40 ± 0.68	3.28 ± 0.16	2.26 ± 0.24	0.08/0.22	+	BSMAM (sigmab 26 ± 7%, OD 23%)
6	20°36.026′S	66°53.341′W	NCL-5114054	8.36 ± 0.81	3.56 ± 0.14	2.35 ± 0.25	0.08/0.23	++	BSMAM (sigmab 18 ± 3%, OD 21%)
7	20°35.949′S	66°53.440′W	NCL-5114055	9.24 ± 0.88	5.40 ± 0.23	1.71 ± 0.18	0.06/0.17	+	BSMAM (sigmab 18 ± 3%, OD 27%)
8a	20°35.698′S	66°54.317′W	NCL-5114058	4.42 ± 0.74	4.37 ± 0.19	1.01 ± 0.17	0.03/0.17	+	BSMAM (sigmab 18 ± 3%, OD 22%)
8b	20°35.721′S	66°53.531′W	NCL-5112112	2.91 ± 0.58	3.08 ± 0.14	0.95 ± 0.19	0.03/0.19	+	BSMAM (sigmab 26 ± 7%, OD 39%)
9	20°33.785′S	66°52.300′W	NCL-5114059	*4.69 ± 0.85*	*4.48 ± 0.17*	*1.05 ± 0.19*	*0.03/0.19*	−	*BSMAM (sigmab 18 ± 3%, OD 33%)*
10a	20°35.138′S	66°52.213′W	NCL-5112113	*2.38 ± 0.72*	*3.02 ± 0.14*	*0.79 ± 0.24*	*0.03/0.24*	−	*BSMAM (sigmab 26 ± 7%, OD 55%)*
10b	20°33.780′S	66°52.481′W	NCL-5112114	2.18 ± 0.30	3.74 ± 0.16	0.58 ± 0.08	0.02/0.08	+	BSMAM (sigmab 26 ± 7%, OD 54%)
11	20°34.582′S	66°52.812′W	NCL-5112115	1.69 ± 0.33	3.18 ± 0.15	0.53 ± 0.11	0.02/0.11	+	BSMAM (sigmab 26 ± 7%, OD 54%)
12	20°35.226′S	66°51.964′W	NCL-5114061	*2.61 ± 0.54*	*4.21 ± 0.18*	*0.62 ± 0.13*	*0.02/0.13*	−	*BSMAM (sigmab 18 ± 3%, OD 50%)*

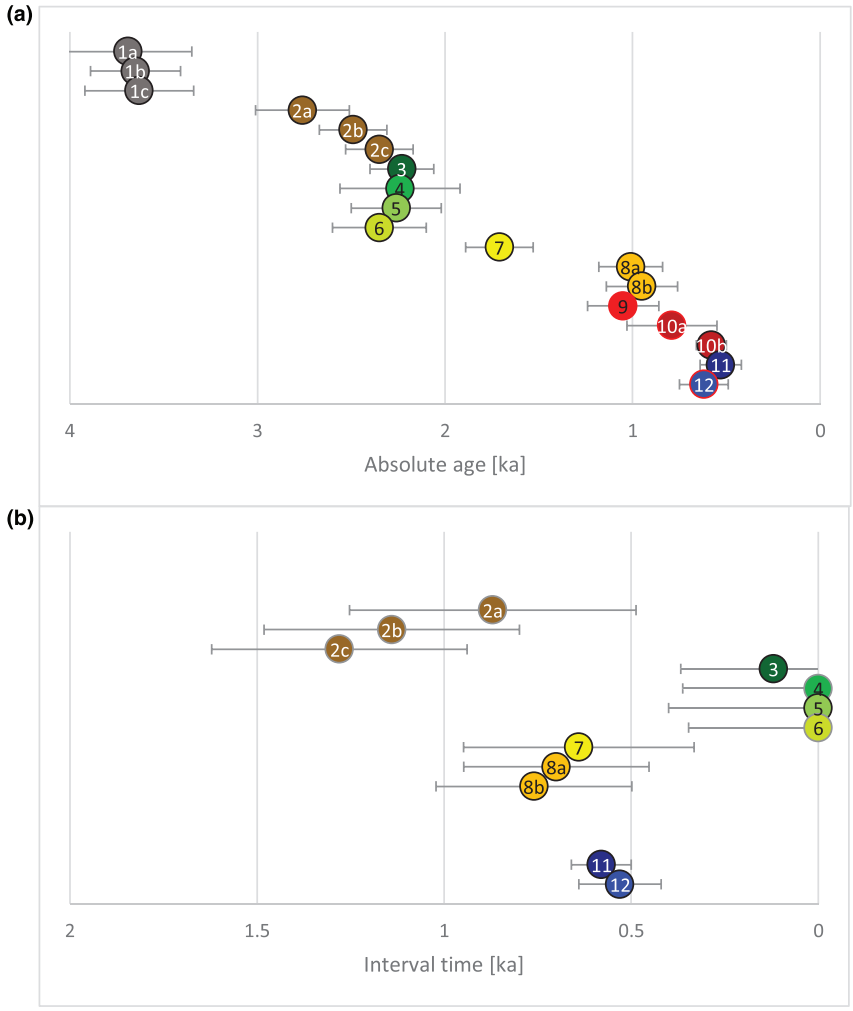

FIGURE 11 (a) OSL age for each of the dated samples, with 1-sigma standard error. (b) Interval time between consecutive channel belts based on OSL ages. Colour coding of sample numbers as in Figure 6

TABLE 2 Interval time and metrics for river sinuosity (SI) and alluvial-ridge aggradation. Interval type denoted 'av' (inter-avulsion period), 'max' (maximum value), or 'err' (unreliable data: in italics)

				SI		Ridge aggradation	
Sample	Type	Inter-avulsion period [ky]	L-trunc	[–]	[–/ka]	[cm]	[cm/ka]
1a	max	9.02 ± 1.54	0%	1.76	0.08		
1b	max	9.06 ± 1.52	0%	1.75	0.08		
1c	max	9.08 ± 1.53	0%	2.24	0.14		
2a	max	0.87 ± 0.38	1%	2.56	1.79		
2b	max	1.14 ± 0.34	0%	2.03	0.90		
2c	max	1.28 ± 0.34	0%	1.85	0.66		
3	av	0.12 ± 0.25	31%	1.85	7.08		
4	max	−0.01 ± 0.36	51%	1.82	0.00		
5	av	−0.02 ± 0.40	52%	2.28	0.00		
6	max	−0.09 ± 0.35	60%	1.88	0.00		
7	av	0.64 ± 0.31	2%	1.25	0.39	25	39
8a	av	0.70 ± 0.25	0%	1.70	1.00	28	40
8b	av	0.76 ± 0.26	0%	1.70	0.92	28	37
9	*err*	*−0.10 ± 0.27*	*65%*	*1.41*	*0.00*		
10a	*err*	*0.26 ± 0.31*	*20%*	*1.75*	*2.88*		
10b	*err*	*0.47 ± 0.21*	*1%*	*1.75*	*1.60*		
11	av	0.58 ± 0.08	0%	1.36	0.62	30	52
12	av	0.53 ± 0.11	0%	1.29	0.55	24	45

Channel belt 6 originated from avulsion point C. The river flowed to the west, then turned southwest (Figure 6) and again to the west beyond the study area. The abandonment age in sample 6 is 2.35 ± 0.25 ka (Table 1 and Figure 11a). Note that the mean abandonment age is older than that of channel belt 5, hence resulting in a negative interval time and likeliness of coevality.

Channel belt 7 is a narrow (0.19 km wide), poorly developed channel belt formed by a low-sinuosity channel (SI = 1.25) that branched off from meandering channel 6 at avulsion point D, to flow towards the west (Figure 6). Upstream from the avulsion point, the channel has hardly modified the deposits of the former channel. Sample 7 shows an abandonment age of 1.71 ± 0.18 ka (Table 1 and Figure 11a), which results in an inter-avulsion period of 0.64 ± 0.31 ka (Table 2 and Figure 11b).

Channel belt 8 originated from avulsion point E with a palaeoflow direction towards the west. Upstream of the avulsion point, the channel reused and enlarged point bars of the older channel belt complex 6–7 by expansion, downstream migration, and rotation, to form large single-point bars (Figure 6). Two samples (8a and 8b) show similar ages of abandonment, the youngest of which is 0.95 ± 0.19 ka (Table 1 and Figure 11a). This yields an inter-avulsion period of 0.76 ± 0.26 ka (Table 2 and Figure 11b).

Channel belt 9 is narrow (0.2 km wide) and comprises a low-sinuous river (SI = 1.41) that diverted from channel belt 8 at avulsion point F. A small part of the river path is overprinted by the modern river. The palaeoflow direction of this channel belt is due north (Figure 6). The OSL age of sample 9 (1.05 ± 0.19 ka) is judged to be unreliable based on the large scatter in equivalent doses, hence the absolute abandonment age cannot be established (Table 1 and Figure 11a).

Channel belt 10 originated from local avulsion point F and flowed parallel to channel belt 9 towards the north (Figure 6). The river rejoined river path 9 at the northern edge of the study area, reusing the existing channel depression. Both channel belts have a remnant, perched, hanging thalweg in their sections north of the current river, suggesting that they are (partially) reoccupied during peak-discharge conditions. Sample 10b shows an abandonment age of 0.58 ± 0.08 ka (Table 1 and Figure 6b).

Channel belt 11 diverted from 10 at avulsion point G (Figure 6), flowed to the north-northwest, and beyond the partial truncation point of channel belt 3, occupied the depression between alluvial ridges of channel belts 2 and 3. Upstream of the avulsion point, the channel has remodelled and enlarged point bars of previous channel belt 10. The channel has not yet been fully abandoned and can be reactivated in peak-discharge periods up to the present day (Figures 8b and 9). The channel has been active for 0.58 ± 0.08 ka (sample 10b; Table 1 and Figure 11a). Sample 11 is indicative of the most recent lateral accretion, dated at 0.53 ± 0.11 ka (Table 1 and Figure 11a).

The present-day river forms channel belt 12 and diverted from channel belt 11 at local avulsion point H (Figure 6). The river trajectory has an anastomosing pattern, rejoining river path 11 to the north-northwest. Sample 12 captures the first accretion of the channel near its avulsion point H but yields unreliable results (Table 1 and Figure 11a). Beyond avulsion point H, the previous river path 11 is reactivated during peak discharge (Figures 8d and 9), which shows that the avulsion is gradual and ongoing.

4.3 | Avulsion frequency, inter-avulsion period, and active migration time

The interval time between successive avulsions in the study area was quantified by using the reconstructed absolute geochronology of channel belts in the study area.

Channel belts 3, 5, 7, and 8 have a clearly defined period between their abandonment age and that of their precursor (Table 2 and Figure 11b), ranging from −0.02 ± 0.40 ka (channel belt 5) to 0.76 ± 0.26 ka (channel belt 8). Other channel belts show equivalent time intervals of up to 1.28 ± 0.34 ka (channel belt 2), although these should be perceived as maximum values due to the ambiguity of their precursors. Several channel belts show overlapping inter-avulsion ages (Figure 11a), such as channel belt 12 (sample taken at the first, not last, lateral accretion surface), which has a slightly older median age of 0.62 ± 0.13 ka compared to the last phase of sedimentation in channel belt 11, with a median age of 0.53 ± 0.11 ka.

The active migration rate (Table 3) in the different channel belts (i.e. the point-bar expansion per year) ranges from 0.7 to 2.5 m/y. Compared with the OSL inter-avulsion timescale, the migration times show that the channels are active only in part of the avulsion period, which is related to the dryland climate setting of the Altiplano Basin, in which point-bar expansion is limited to low-frequency, high-magnitude peak-discharge periods (Donselaar et al., 2013; Li, 2014).

5 | DISCUSSION

5.1 | Morphodynamic model

After avulsion, each new river path started as a single-thread, low-sinuous channel that increased its sinuosity over time by lateral growth of point bars, thereby widening its channel belt, as witnessed by the expansion left and right of successive point bars from its initial attachment location on the adjacent floodplain (i.e. the start position after avulsion; see e.g. channel belt 10 in Figure 6). The final, preserved point-bar morphology is the end product of: (a) point-bar expansion, rotation, and downstream migration prior to avulsion; and (b) the river capacity to enlarge or truncate, after avulsion, pre-existing point bars upstream from each avulsion point. The process of progressive meandering implies that channel sinuosity and point-bar dimensions are proportional to the duration of channel activity. This observation is in line with the morphodynamic model presented for the similarly sinuous and non-vegetated fluvial fan of the McLeod Springs Wash in the endorheic Toiyabe Basin of Nevada, USA (Ielpi & Lapôtre, 2019).

Upstream of the avulsion point, each new river path inherited the path of the avulsed parent channel. Two end members are observed in the geomorphological evolution of the new river paths. (a) Downstream of the avulsion point (e.g. avulsion from channels 2 to 3 and from 6 to 7), the new river path developed a small and narrow (0.2 to 0.4 km wide) channel belt (channel belts 3 and 7) with a relatively low sinuosity (SI = 1.25–1.58); upstream of the avulsion, the point bars are not modified by expansion or truncation, as witnessed by the similarity between SI of the avulsed parent channel downstream and the channel upstream from the avulsion point. (b) The new channel further expanded and/or truncated the point bars of the

TABLE 3 Inferred active migration time of the channel belts based on the power-law correlation of (average) channel width and migration rate for unvegetated rivers (figure 2a in Ielpi & Lapôtre, 2020) and point-bar morphometrics (maximum radius). Activity is expressed as a percentage of total OSL-based interval and cannot exceed 100%. Note that only activity-% in bold is based on type 'av' (Table 2) interval times (i.e. relatively most representative) and that error cannot be established analytically. Unreliable data are in italics

Channel belt no.	Point-bar radius [m]	Channel width [m]	Migration rate [m/y]	Migration time [y]	OSL inter-avulsion period [ky]	Activity [%]
1a	326	18	1.5	217	8.96 ± 1.48	2%
1b	579	34	2.5	232	9.01 ± 1.46	3%
1c	516	24	1.9	272	9.01 ± 1.46	3%
2a	388	13	1.1	353	0.87 ± 0.35	41%
2b	570	13	1.1	518	1.13 ± 0.31	46%
2c	520	15	1.3	400	1.27 ± 0.30	31%
3	255	11	1.3	196	0.12 ± 0.20	**100%**
4	364	16	1.3	280	−0.02 ± 0.26	100%
5	481	16	1.3	370	0.03 ± 0.37	**100%**
6	391	18	1.5	261	−0.12 ± 0.38	100%
7	101	10	0.9	112	0.64 ± 0.28	**18%**
8a	459	19	1.5	306	0.71 ± 0.24	**43%**
8b	587	18	1.5	391	0.77 ± 0.25	**51%**
9	*116*	*8*	*0.7*	*166*	*−0.10 ± 0.26*	*err*
10a	*302*	*13*	*1.1*	*275*	*0.28 ± 0.30*	*err*
10b	*478*	*14*	*1.2*	*398*	*0.46 ± 0.20*	*err*
11	146	20	1.6	91	0.59 ± 0.13	**15%**
12	229	24	1.9	121	0.53 ± 0.11	**23%**

parent channel upstream of the avulsion point (e.g. avulsion from channel complex 6–7 to 8) and developed a mature meandering channel belt (width up to 1 km, SI = 1.70) downstream of the avulsion point. Channel 11 shows an intermediate development, with expansion of the point bars of channel 10 upstream from avulsion point G. The different morphological development of the avulsion channels is conditioned by the discharge that the avulsion channel diverted from the parent channel (partial or total avulsion), and by the time that the avulsion channel had to develop its meander belt. Channel 7 is considered as a partial avulsion of channel 6, while channel 8 represents a total avulsion channel of the channel complex 6–7.

Consecutive channel belts are organized in an overall radial pattern (Figure 6) of alluvial ridges, each of which has a positive morphology (Figure 10). The channel-belt geochronology shows that the resultant depositional architecture is formed by compensational stacking where—after avulsion—the new channel avoided the positive alluvial-ridge relief of its precursors. Alluvial ridges may onlap onto adjacent pre-existing ridges (Figure 10). Compensational stacking is more prominent in the proximal part of the radial pattern of the river system, where successive avulsions and occasional channel-belt cannibalization of precursory channel belts over time have formed a large interconnected sheet of amalgamated channel deposits. Lateral amalgamation of alluvial ridges resulted in a wide area of positive relief on the floodplain (Figure 10). The high-resolution dGPS profile (Figure 10) shows the subtle elevation profiles of alluvial ridges corresponding to channel belts 6–7, 8, 11, and 12, respectively. The (residual) channels are perched on the crests, and the topographic slope on either side corresponds to the accumulation of amalgamated levee and crevasse-splay sediments (Figure 10). The areas in between adjacent ridges are elevated higher than the initial floodplain level, which suggests that the inter-channel-belt depressions received sediment from both successive rivers, resulting in onlapping of crevasse-splay deposits within the laterally confined space. The preserved relief is 25–31 cm above the adjacent floodplain (i.e. the local minimum), translating into vertical aggradation rates ranging from 0.37 to 0.52 m/ka (Table 2). Note that the elevation of abandoned alluvial ridges (channel belts 6–7 and 8 in Figure 10) may have been reduced by deflation, notably after the 2009 and 2010 dust storms (Gaiero et al., 2013) and by compaction as the channel belts became moribund after avulsion, and that the adjacent floodplain may have been lower at time of deposition. Hence, the vertical aggradation rates should be regarded as minimum values.

Towards the terminus of the river system, the channel belts diverge over the unconfined floodplain space. Cannibalism is therefore less likely to occur and the individual belts have a high preservation potential. The resulting depositional architecture of the Río Colorado dryland river system is a laterally extensive sheet with a fan-shaped top view and a convex-up shape in a cross-section perpendicular to the flow trend, made up of radially arranged, connected sandy alluvial ridges that encompass floodplain silt.

In unconfined prograding dryland river systems such as the Río Colorado, the vertical aggradation of channel-lag sand is interpreted to be directly proportional to levee and crevasse-splay sedimentation (van Toorenenburg et al., 2016). As the alluvial-ridge aggradation continued, the channel levees were increasingly perched above the surrounding floodplain (i.e. channel super-elevation). The along-river gradient decreased in the process, whereas the cross-floodplain gradient increased (Figure 10), thus creating a gradient advantage for the river to break out of its course by levee crevassing and switching to a hydrodynamically more favourable, steeper path. The minimum

aggradation rates to reach the threshold of super-elevation in this study are of the same order as presented by Ganti et al. (2016).

5.2 | Gradual avulsion

Several channel belts show a clustering and overlap in OSL sample age. Notably channel belts 3 to 6, 8 and 9, and 10 to 12 (Figure 11a). In part, the overlap can be explained by the standard error of the sample age, but coeval activity of more than one channel belt cannot be ruled out. It should be noted that the inter-avulsion period is only equal to the duration of channel-belt activity when avulsions are abrupt and complete. The mechanism for avulsion proposed by van Toorenenburg et al. (2018) suggests that progradational avulsions in the study area are gradual. This implies that channel belts in the study area are active for a longer period of time than their respective inter-avulsion period and that channel abandonment follows some time after avulsion. This assumption is supported by direct observation at the avulsion location of the last-abandoned channel belt 11 (Figure 8d), where the median age of 0.62 ± 0.13 ka for the start of channel belt 12 (sample taken at the first, not last, lateral accretion surface) is slightly older than the last phase of sedimentation in channel 11 (0.53 ± 0.11 ka). At peak discharge, part of the total water volume is diverted at the avulsion location into the remnant depression of the inactive old channel. Flow diversion leads to a decrease in flow energy in the active channel and the formation of a sediment threshold at the entry of the old channel by deposition of ripple-laminated very fine sand (Figures 8d and e). As a consequence, the threshold aggrades at the avulsion point at each successive peak discharge until the threshold aggradation will effectively close off the entrance. Until that time, technically speaking the new parent channel and the avulsed channel section will both be active, but only in the short (∼days) peak discharge period, and not as a coeval system of multiple, coexisting fluvial channels as in the concept of distributive fluvial systems (DFS; cf. Weissmann et al., 2010 and the discussion of DFS by Fielding et al., 2012), but rather as a fluvial system with an anastomosing pattern, caused by the gradual abandonment of the avulsed channels in a low-gradient floodplain setting (Makaske, 2001).

The migration rates of the channel belts in the present study have a smaller range than those presented by Ielpi and Lapôtre (2020; see online Supplementary Information) for the Río Colorado (Table 4). The difference in the upper limit of the migration rate is explained by the smaller amount of data points in the present study, and by the differences in measuring methods of river-channel widths (on-the-ground measurements in this study, and satellite-imagery analysis in Ielpi & Lapôtre, 2020). The OSL sample ages show a time period with a minimum duration in the order of 1 ka between the end of activity of channel belt 6 (at 2.35 ± 0.25 ka) and the start of channel belt 8 (at 1.01 ± 0.17 ka; Figure 11a and Table 1). In this period, the only recorded channel is the small channel belt 7, characterized by a low SI of 1.25 (Table 2), by the development of only a narrow channel belt (Figure 6) in its long inter-avulsion life of 0.64 ± 0.31 ka (Table 2), and by the short active migration time of 0.112 ka (Table 3). In combination, these data suggest a prolonged drop in river discharge (activity <20% of the total inter-avulsion time, Table 3), possibly related to long-term dry periodicity in the El Niño Southern Oscillation (ENSO) circulation system (Bräuning, 2009). This hypothesis is supported by the interpretation of Baucom and Rigsby (1999), who related fluvial downcutting of the Río Desaguadero in the northern part of the Altiplano Basin, dated at 2.0 ka, with decreased effective moisture during a dry climate period. Channel belts 11 and 12 show a similarly low activity ratio and SI, corresponding to the current dry period in ENSO (figure 2c in Bräuning, 2009).

TABLE 4 Migration rate and channel width ranges of the Río Colorado from Ielpi and Lapôtre (2020) and the present study

	Ielpi and Lapôtre (2020)	Present study
Migration rate [m/y]	0.8–6.5	0.7–2.5
Channel width [m]	5.8–34.2	8.0–34.0
Data points	54	18

6 | CONCLUSIONS

This study yields the spatio-temporal reconstruction of the avulsion history and channel-belt depositional architecture in the modern Río Colorado dryland river system (Altiplano Basin, Bolivia), based on the integrated analysis of satellite imagery, ground-truth fieldwork observations of fluvial sedimentology and geomorphology, and OSL age determination.

In a maximum timespan of 12.7 ± 1.5 ka, the Río Colorado formed a sediment sheet with a fan-shaped, convex-up geomorphology covering approximately 500 km^2, with a maximum observed thickness of 3 m. Consecutive channel belts in the river system are organized in an overall radial pattern of juxtaposed alluvial ridges, each of which has a positive morphology. The channel-belt geochronology shows that the resultant depositional architecture is formed by compensational stacking where, after avulsion, the new channel avoided the alluvial-ridge relief of its precursors. In the proximal part of the dryland river system, onlap of overbank sediments resulted in lateral amalgamation of adjacent alluvial ridges and partial cannibalization of precursory fluvial sediments. This created an interconnected sheet of fluvial sand deposits, forming a large area of positive relief. Further downstream, towards the river terminus, the channel belts diverged over the unconfined floodplain space, and the individual alluvial ridges have a high preservation potential. The minimum vertical sediment accretion rate of the alluvial ridges ranges from 0.37 to 0.52 m/ka.

Avulsions of the meandering Río Colorado have an inter-avulsion period up to 1.28 ± 0.34 ka. After avulsion, a new river path started as a low-sinuous, single-thread channel in a narrow belt, which in time expanded its width by lateral accretion of point bars, attaining an increase of SI by 0–7 per thousand years. The OSL sample age of several successive channel belts shows clustering and time overlap, which can in part be explained by the standard error of the sample age. Direct observation at the most recent avulsion location shows that the avulsed river channel may still receive water by flow diversion in peak discharge periods, and that an aggradational sediment threshold forms at the entrance of the avulsed channel. The long time interval from 2.35 ± 0.25 ka to 1.01 ± 0.17 ka, in which only a narrow channel belt is formed by a low-sinuous river with a low migration

rate of 0.9 m/y, is interpreted as the result of low river discharge related to long-term dry periodicity in the ENSO circulation system.

Multiple avulsions are concentrated in the same area, suggesting a near-nodal avulsion form for the development of the Río Colorado dryland river system. The most recent river paths (channel belts 9–12) suggest an anastomosing pattern for these channels with moderate sinuosity (SI = 1.29–1.75). In contrast, the older large channels are highly sinuous (SI = 1.70–2.56). The change of pattern from highly sinuous channels to anastomosing channels with a lower sinuosity suggests a change of conditions in time, either in the gradient of the area or in river discharge.

ACKNOWLEDGEMENTS

Sebastian Moyano (Universidad Nacional de Tucumán, Argentina) is thanked for his assistance with the OSL sample acquisition and organization of the fieldwork logistics. Niels Noordijk (TU Delft), Rosmar Villegas Mendoza and Carlos Víctor Jiménez Poma (Universidad Mayor de San Andrés - UMSA, La Paz, Bolivia) assisted with the data acquisition. Christian Perdomo Figueroa (TU Delft) participated in the dGPS data acquisition in the 2016 fieldwork as part of his MSc thesis project. Oswaldo Ramos (UMSA) is acknowledged for logistical support. Gert Jan Weltje (KU Leuven) is gratefully acknowledged for challenging the conventional use and presentation of age data. Hans van der Marel (TU Delft) is thanked for assistance with the dGPS data processing, and Santosh Kumar (TU Delft) for his help with the Landsat imagery. Financial support for the research from Wintershall Noordzee B.V., Energie Beheer Nederland (EBN), and ENGIE E&P Nederland B.V. is gratefully acknowledged. Alice Versendaal of the Netherlands Centre for Luminescence dating (NCL) at Wageningen University is thanked for the OSL measurements and analyses. The authors are grateful for the constructive reviews by Alessandro Ielpi and an anonymous reviewer.

CONFLICT OF INTEREST

The authors declare that they have no known competing financial interests or personal relationships that could have appeared to influence the work reported in this paper.

AUTHOR CONTRIBUTIONS

MED: Conceptualization, funding acquisition, methodology, investigation (data collection and formal analysis), supervision, writing – original draft. **MCCG**: Conceptualization, methodology, investigation (data collection and formal analysis), writing – review and editing. **KAvT**: Methodology, investigation (data collection and formal analysis), writing – review and editing. **JW**: Methodology, investigation (data processing), writing – review and editing.

DATA AVAILABILITY STATEMENT

The data that support the findings of this study are available on request from the corresponding author.

ORCID

Marinus E. Donselaar https://orcid.org/0000-0003-3509-8856
Koen A. van Toorenenburg https://orcid.org/0000-0003-0616-0198

REFERENCES

Argollo, J. & Mourguiart, P. (2000) Late Quaternary climate history of the Bolivian Altiplano. *Quaternary International*, 72(1), 37–51. Available from: https://doi.org/10.1016/S1040-6182(00)00019-7

Aslan, A., Autin, W.J. & Blum, M.D. (2005) Causes of river avulsion: Insights from the Late Holocene avulsion history of the Mississippi River, U.S.A. *Journal of Sedimentary Research*, 75(4), 650–664. Available from: https://doi.org/10.2110/jsr.2005.053

Baker, P.A., Rigsby, C.A., Seltzer, G.O., Fritz, S.C., Lowenstein, T.K., Bacher, N.P. & Veliz, C. (2001) Tropical climate changes at millennial and orbital timescales on the Bolivian Altiplano. *Nature*, 409(6821), 698–701. Available from: https://doi.org/10.1038/35055524

Baucom, P.C. & Rigsby, C.A. (1999) Climate and lake-level history of the northern Altiplano, Bolivia, as recorded in Holocene sediments of the Rio Desaguadero. *Journal of Sedimentary Research*, 69(3), 597–611. Available from: https://doi.org/10.2110/jsr.69.597

Berendsen, H.J.A. & Stouthamer, E. (2000) Late Weichselian and Holocene palaeogeography of the Rhine–Meuse delta. *Palaeogeography, Palaeoclimatology, Palaeoecology*, 161(3–4), 311–335. Available from: https://doi.org/10.1016/S0031-0182(00)00073-0

Bills, B.G., de Silva, S.L., Currey, D.R., Emenger, R.S., Lillquist, K.D., Donnellan, A. & Worden, B. (1994) Hydro-isostatic deflection and tectonic tilting in the central Andes: Initial results of a GPS survey of Lake Minchin shorelines. *Geophysical Research Letters*, 21(4), 293–296. Available from: https://doi.org/10.1029/93GL03544

Bräuning, A. (2009) Climate variability of the tropical Andes since the late Pleistocene. *Advances in Geosciences*, 22, 13–25. Available from: https://doi.org/10.5194/adgeo-22-13-2009

Brice, J.C. (1974) Evolution of meander loops. *Geological Society of America Bulletin*, 85(4), 581–586. Available from: https://doi.org/10.1130/0016-7606(1974)85<581:EOML>2.0.CO;2

Bridge, J.S. (2006) Fluvial facies models: Recent developments. *SEPM Special Publication*, 84, 85–170. Available from: https://doi.org/10.2110/pec.06.84.0085

Bristow, C.S., Smith, N. & Rogers, J. (1999) Gradual avulsion, river metamorphosis and reworking by underfit streams: a modern example from the Brahmaputra River in Bangladesh and a possible ancient example in the Spanish Pyrenees. In: Smith, N.D. & Rogers, J. (Eds.), *Fluvial Sedimentology VI*, Special Publications of the International Association of Sedimentologists. Oxford: Blackwell; 28, 221–230.

Bull, L.J. & Kirkby, M.J. (2002) Dryland river characteristics and concepts. In: Bull, L.J. & Kirkby, M.J. (Eds.) *Dryland Rivers: Hydrology and Geomorphology of Semi-Arid Channels*. Chichester: Wiley, pp. 3–15.

Chakraborty, T., Kar, P., Ghosh, P. & Basu, S. (2010) Kosi Megafan: Historical records, geomorphology and the recent avulsion of the Kosi River. *Quaternary International*, 227(2), 143–160. Available from: https://doi.org/10.1016/j.quaint.2009.12.002

Chepstow-Lusty, A., Bush, M.B., Frogley, M.R., Baker, P.A., Fritz, S.C. & Aronson, J. (2005) Vegetation and climate change on the Bolivian Altiplano between 108,000 and 18,000 years ago. *Quaternary Research*, 63(1), 90–98. Available from: https://doi.org/10.1016/j.yqres.2004.09.008

Cohen, K.M., Gouw, M.J.P. & Holten, J.P. (2005) Fluvio-deltaic floodbasin deposits recording differential subsidence within a coastal prism (central Rhine–Meuse delta, The Netherlands). *Special Publications of the International Association of Sedimentologists*, 35, 295–320.

Coronel, M.D., Isla, M.F., Veiga, G.D., Mountney, N.P. & Colombera, L. (2020) Anatomy and facies distribution of terminal lobes in ephemeral fluvial successions: Jurassic Tordillo Formation, Neuquén Basin, Argentina. *Sedimentology*, 67(5), 2596–2624. Available from: https://doi.org/10.1111/sed.12712

Costa, A.C., Bronstert, A. & de Araújo, J.C. (2012) A channel transmission losses model for different dryland rivers. *Hydrology and Earth System*

Sciences, 16(4), 1111–1135. Available from: https://doi.org/10.5194/hess-16-1111-2012

Costa, A.C., Foerster, S., de Araújo, J.C. & Bronstert, A. (2013) Analysis of channel transmission losses in a dryland river reach in north-eastern Brazil using streamflow series, groundwater level series and multi-temporal satellite data. *Hydrological Processes*, 27(7), 1046–1060. Available from: https://doi.org/10.1002/hyp.9243

Cunningham, A.C. & Wallinga, J. (2012) Realizing the potential of fluvial archives using robust OSL chronologies. *Quaternary Geochronology*, 12, 98–106. Available from: https://doi.org/10.1016/j.quageo.2012.05.007

Cunningham, A.C., Wallinga, J. & Minderhoud, P.S.J. (2011) Expectations of scatter in equivalent-dose distributions when using multi-grain aliquots for OSL dating. *Geochronometria*, 38(4), 424–431. Available from: https://doi.org/10.2478/s13386-011-0048-z

Daniel, J.F. (1971) Channel movement of meandering Indiana streams. *Geological Survey Professional Paper*, 732-A, 1–18.

Donselaar, M.E., Cuevas Gozalo, M.C. & Moyano, S. (2013) Avulsion processes at the terminus of low-gradient semi-arid fluvial systems: Lessons from the Río Colorado, Altiplano endorheic basin, Bolivia. *Sedimentary Geology*, 283, 1–14. Available from: https://doi.org/10.1016/j.sedgeo.2012.10.007

Edmonds, D.A., Hajek, E.A., Downton, N. & Bryk, A.B. (2016) Avulsion flow-path selection on rivers in foreland basins. *Geology*, 44(9), 695–698. Available from: https://doi.org/10.1130/G38082.1

Elger, K., Oncken, O. & Glodny, J. (2005) Plateau-style accumulation of deformation: Southern Altiplano. *Tectonics*, 24(4), TC4020. Available from: https://doi.org/10.1029/2004TC001675

Ethridge, F.G., Skelly, R.L. & Bristow, C.S. (1999) Avulsion and crevassing in the sandy, braided Niobrara River: Complex response to base-level rise and aggradation. In: Smith, N.D. & Rogers, J. (Eds.) *Fluvial Sedimentology VI*, Special Publications of the International Association of Sedimentologists, Vol. 28. Oxford: Blackwell, pp. 179–191.

Fielding, C.R., Ashworth, P.J., Best, J.L., Prokocki, E.W. & Sambrook Smith, G.H. (2012) Tributary, distributary and other fluvial patterns: What really represents the norm in the continental rock record? *Sedimentary Geology*, 261–262, 15–32. Available from: https://doi.org/10.1016/j.sedgeo.2012.03.004

Flood, Y.S. & Hampson, G.J. (2014) Facies and architectural analysis to interpret avulsion style and variability: Upper Cretaceous Blackhawk Formation, Wasatch Plateau, Central Utah, USA. *Journal of Sedimentary Research*, 84(9), 743–762. Available from: https://doi.org/10.2110/jsr.2014.59

Fornari, M., Risacher, F. & Féraud, G. (2001) Dating of paleolakes in the central Altiplano of Bolivia. *Palaeogeography, Palaeoclimatology, Palaeoecology*, 172(3–4), 269–282. Available from: https://doi.org/10.1016/S0031-0182(01)00301-7

Gaiero, D.M., Simonella, L., Gassó, S., Gili, S., Stein, A.F., Sosa, P., Becchio, R., Arce, J. & Marelli, H. (2013) Ground/satellite observations and atmospheric modeling of dust storms originating in the high Puna-Altiplano deserts (South America): Implications for the interpretation of paleo-climatic archives. *Journal of Geophysical Research: Atmospheres*, 118(9), 3817–3831. Available from: https://doi.org/10.1002/jgrd.50036

Galbraith, R.F., Roberts, R.G., Laslett, G.M., Yoshida, H. & Olley, J.M. (1999) Optical dating of single and multiple grains of quartz from Jinmium rock shelter, northern Australia. Part I: Experimental design and statistical models. *Archaeometry*, 41(2), 339–364. Available from: https://doi.org/10.1111/j.1475-4754.1999.tb00987.x

Ganti, V., Chadwick, A.J., Hassenruck-Gudipati, H.J. & Lamb, M.P. (2016) Avulsion cycles and their stratigraphic signature on an experimental backwater-controlled delta. *Journal of Geophysical Research: Earth Surface*, 121(9), 1651–1675. Available from: https://doi.org/10.1002/2016JF003915

Ganti, V., Chu, Z., Lamb, M.P., Nittrouer, J.A. & Parker, G. (2014) Testing morphodynamic controls on the location and frequency of river avulsions on fans versus deltas: Huanghe (Yellow River), China. *Geophysical Research Letters*, 41(22), 7882–7890. Available from: https://doi.org/10.1002/2014GL061918

Ganti, V., Whittaker, A.C., Lamb, M.P. & Fischer, W.W. (2019) Low-gradient, single-threaded rivers prior to greening of the continents. *PNAS*, 116(24), 11652–11657. Available from: https://doi.org/10.1073/pnas.1901642116

Garreaud, R.D., Vuille, M. & Clement, A.C. (2003) The climate of the Altiplano: Observed current conditions and mechanisms of past changes. *Palaeogeography, Palaeoclimatology, Palaeoecology*, 194(1–3), 5–22. Available from: https://doi.org/10.1016/S0031-0182(03)00269-4

Grosjean, M. (1994) Paleohydrology of the Laguna Lejía (north Chilean Altiplano) and climatic implications for late-glacial times. *Palaeogeography, Palaeoclimatology, Palaeoecology*, 109, 89–100. Available from: https://doi.org/10.1016/0031-0182(94)90119-8

Hajek, E.A. & Edmonds, D.A. (2014) Is river avulsion controlled by floodplain morphodynamics. *Geology*, 42(3), 199–202. Available from: https://doi.org/10.1130/G35045.1

Hajek, E.A. & Wolinsky, M.A. (2012) Simplified process modeling of river avulsion and alluvial architecture: Connecting models and field data. *Sedimentary Geology*, 257–260, 1–30. Available from: https://doi.org/10.1016/j.sedgeo.2011.09.005

He, L., Amorosi, A., Ye, S., Xue, C., Yang, S. & Laws, E.A. (2020) River avulsions and sedimentary evolution of the Luanhe fan-delta system (North China) since the late Pleistocene. *Marine Geology*, 425, 106194. Available from: https://doi.org/10.1016/j.margeo.2020.106194

Heller, P.L. & Paola, C. (1996) Downstream changes in alluvial architecture: An exploration of controls on channel stacking patterns. *Journal of Sedimentary Research*, 66, 297–306. Available from: https://doi.org/10.1306/D4268333-2B26-11D7-8648000102C1865D

Horton, B.K., Hampton, B.A. & Waanders, G.L. (2001) Paleogene synorogenic sedimentation in the Altiplano Plateau and implications for initial mountain building in the Central Andes. *Geological Society of America Bulletin*, 113(11), 1387–1400. Available from: https://doi.org/10.1130/0016-7606(2001)113%3C1387:PSSITA%3E2.0.CO;2

Ielpi, A. (2019) Morphodynamics of meandering streams devoid of plant life: Amargosa River, Death Valley, California. *Geological Society of America Bulletin*, 31(5–6), 782–802. Available from: https://doi.org/10.1130/B31960.1

Ielpi, A., Fralick, P., Ventra, D., Ghinassi, M., Lebeau, L.E., Marconato, A., Meek, R. & Rainbird, R.H. (2018) Fluvial floodplains prior to greening of the continents: Stratigraphic record, geodynamic setting, and modern analogues. *Sedimentary Geology*, 372, 140–172. Available from: https://doi.org/10.1016/j.sedgeo.2018.05.009

Ielpi, A., Ghinassi, M., Rainbird, R.H. & Ventra, D. (2018) Planform sinuosity of Proterozoic rivers: A craton to channel-reach perspective. In *Fluvial Meanders and their Sedimentary Products in the Rock Record*, Ghinassi M, Colombera L, Mountney NP, Reesink AJH (eds). Blackwell: Oxford; 81–118. https://doi.org/10.1002/9781119424437.ch4

Ielpi, A. & Lapôtre, M.G.A. (2019) Barren meandering streams in the modern Toiyabe Basin of Nevada, U.S.A., and their relevance to the study of the pre-vegetation rock record. *Journal of Sedimentary Research*, 89, 399–415. Available from: https://doi.org/10.2110/jsr.2019.25

Ielpi, A. & Lapôtre, M.G.A. (2020) A tenfold slowdown in river meander migration driven by plant life. *Nature Geoscience*, 13(1), 82–86. Available from: https://doi.org/10.1038/s41561-019-0491-7

Jackson, R.G. (1976) Depositional model of point bars in the lower Wabash River. *Journal of Sedimentary Research*, 46, 579–594. Available from: https://doi.org/10.1306/212F6FF5-2B24-11D7-8648000102C1865D

Jarihani, A.A., Larsen, J.R., Callow, J.N., McVicar, T.R. & Johansen, K. (2015) Where does all the water go? Partitioning water transmission losses in a data-sparse, multi-channel and low-gradient dryland river system using modelling and remote sensing. *Journal of Hydrology*, 529, 1511–1529. Available from: https://doi.org/10.1016/j.jhydrol.2015.08.030

Jones, H.L. & Hajek, E.A. (2007) Characterizing avulsion stratigraphy in ancient alluvial deposits. *Sedimentary Geology*, 202(1–2), 124–137. Available from: https://doi.org/10.1016/j.sedgeo.2007.02.003

Jones, H.L. & Schumm, S.A. (1999) Causes of avulsion: An overview. In *Fluvial Sedimentology VI*, Smith ND, Rogers J (eds). Special Publications of the International Association of Sedimentologists, Vol. 28. Blackwell: Oxford; 171–178. https://doi.org/10.1002/9781444304213.ch13

Kleinhans, M.G., Ferguson, R.I., Lane, S.N. & Hardy, R.J. (2013) Splitting rivers at their seams: Bifurcations and avulsion. *Earth Surface Processes and Landforms*, 38(1), 47–61. Available from: https://doi.org/10.1002/esp.3268

Knighton, A.D. & Nanson, G.C. (1994) Flow transmission along an arid zone anastomosing river, Cooper Creek, Australia. *Hydrological Processes*, 8(2), 137–154. Available from: https://doi.org/10.1002/hyp.3360080205

Kraus, M.J. & Wells, T.M. (1999) Recognizing avulsion deposits in the ancient stratigraphical record. In *Fluvial Sedimentology VI*, Smith ND, Rogers J (eds). Special Publications of the International Association of Sedimentologists, Vol. 28. Oxford: Blackwell; 251–268. https://doi.org/10.1002/9781444304213.ch19

Lange, J. (2005) Dynamics of transmission losses in a large arid stream channel. *Journal of Hydrology*, 306(1–4), 112–126. Available from: https://doi.org/10.1016/j.jhydrol.2004.09.016

Larkin, Z.T., Tooth, S., Ralph, T.J., Duller, G.A.T., McCarthy, T., Keen-Zebert, A. & Humphries, M.S. (2017) Timescales, mechanisms, and controls of incisional avulsions in floodplain wetlands: Insights from the Tshwane River, semiarid South Africa. *Geomorphology*, 283, 158–172. Available from: https://doi.org/10.1016/j.geomorph.2017.01.021

Leeder, M.R. (1978) A quantitative stratigraphic model for alluvium, with special reference to channel deposit density and interconnectedness. *Memoirs of the Canadian Society of Petroleum Geologists*, 5, 587–596.

Leopold, L.B. & Wolman, M.G. (1957) River meanders. *Geological Society of America Bulletin*, 71(6), 769–794. Available from: https://doi.org/10.1130/0016-7606(1960)71[769:RM]2.0.CO;2

Li, J. (2014) *Terminal fluvial systems in a semi-arid endorheic basin, Salar de Uyuni (Bolivia)*. PhD thesis, Delft University of Technology.

Li, J., Donselaar, M.E., Hosseini Aria, S.E., Koenders, R. & Oyen, A.M. (2014) Landsat imagery-based visualization of the geomorphological development at the terminus of a dryland river system. *Quaternary International*, 352, 100–110. Available from: https://doi.org/10.1016/j.quaint.2014.06.041

Makaske, B. (2001) Anastomosing rivers: A review of their classification, origin and sedimentary products. *Earth-Science Reviews*, 53(3–4), 149–196. Available from: https://doi.org/10.1016/S0012-8252(00)00038-6

Mohrig, D., Heller, P.L., Paola, C. & Lyons, W.J. (2000) Interpreting avulsion process from ancient alluvial sequences; Guadalope–Matarranya system (northern Spain) and Wasatch Formation (western Colorado). *Geological Society of America Bulletin*, 112, 1787–1803. Available from: https://doi.org/10.1130/0016-7606(2000)112%3C1787:IAPFAA%3E2.0.CO;2

Murray, A.S. & Wintle, A.G. (2003) The single aliquot regenerative dose protocol: Potential for improvements in reliability. *Radiation Measurements*, 37(4–5), 377–381. Available from: https://doi.org/10.1016/S1350-4487(03)00053-2

Nicholas, A.P., Aalto, R.E., Sambrook Smith, G.H. & Schwendel, A.C. (2018) Hydrodynamic controls on alluvial ridge construction and avulsion likelihood in meandering river floodplains. *Geology*, 46(7), 639–642. Available from: https://doi.org/10.1130/G40104.1

Placzek, C., Quade, J. & Patchett, P.J. (2006) Geochronology and stratigraphy of late Pleistocene lake cycles on the southern Bolivian Altiplano: Implications for causes of tropical climate change. *Geological Society of America Bulletin*, 118(5–6), 515–532. Available from: https://doi.org/10.1130/B25770.1

Rigsby, C.A., Bradbury, J.P., Baker, P.A., Rollins, S.M. & Warren, M.R. (2005) Late Quaternary palaeolakes, rivers, and wetlands on the Bolivian Altiplano and their palaeoclimatic implications. *Journal of Quaternary Science*, 20(7–8), 671–691. Available from: https://doi.org/10.1002/jqs.986

Risacher, F. & Fritz, B. (2009) Origin of salts and brine evolution of Bolivian and Chilean salars. *Aquatic Geochemistry*, 15(1–2), 123–157. Available from: https://doi.org/10.1007/s10498-008-9056-x

Schumm, S.A. (1963) Sinuosity of alluvial rivers on the Great Plains. *Geological Society of America Bulletin*, 74(9), 1089–1100. Available from: https://doi.org/10.1130/0016-7606(1963)74[1089:SOAROT]2.0.CO;2

Servant, M., Fournier, M., Argollo, J., Servant-Vildary, S., Sylvestre, F., Wirrmann, D. & Ybert, J.-P. (1995) La dernière transition glaciaire/interglaciaire des Andes tropicales sud (Bolivie) d'après l'étude des variations des niveaux lacustres et des fluctuations glaciaires. *Comptes Rendus de l'Académie Des Sciences, Paris, Séries II*, 320, 729–736.

Sinha, R. (1996) Channel avulsion and floodplain structure in the Gandak–Kosi interfan, north Bihar plains, India. *Zeitschrift für Geomorphologie*, 103, 249–268.

Sinha, R. (2009) The Great avulsion of Kosi on 18 August 2008. *Current Science*, 97, 429–433.

Slingerland, R. & Smith, N.D. (1998) Necessary conditions for a meandering-river avulsion. *Geology*, 26(5), 435–438. Available from: https://doi.org/10.1130/00917613(1998)026%3C0435:NCFAMR%3E2.3.CO;2

Slingerland, R. & Smith, N.D. (2004) River avulsions and their deposits. *Annual Reviews of Earth and Planetary Science*, 32(1), 257–285. Available from: https://doi.org/10.1146/annurev.earth.32.101802.120201

Smith, N.D., Cross, T.A., Dufficy, J.P. & Clough, S.R. (1989) Anatomy of an avulsion. *Sedimentology*, 36(1), 1–23. Available from: https://doi.org/10.1111/j.1365-3091.1989.tb00817.x

Stouthamer, E. & Berendsen, H.J.A. (2001) Avulsion frequency, avulsion duration, and interavulsion period of Holocene channel belts in the Rhine–Meuse Delta, The Netherlands. *Journal of Sedimentary Research*, 71(4), 589–598. Available from: https://doi.org/10.1306/112100710589

Stouthamer, E. & Berendsen, H.J.A. (2007) Avulsion: The relative roles of autogenic and allogenic processes. *Sedimentary Geology*, 198(3–4), 309–325. Available from: https://doi.org/10.1016/j.sedgeo.2007.01.017

Sylvestre, F., Servant, M., Servant-Vildary, S., Causse, C., Fournier, M. & Ybert, J.-P. (1999) Lake-level chronology on the southern Bolivian Altiplano (18°–23°S) during late-glacial time and the early Holocene. *Quaternary Research*, 51(1), 54–66. Available from: https://doi.org/10.1006/qres.1998.2017

Timár, G., Sümegi, P. & Horváth, F. (2005) Late Quaternary dynamics of the Tisza River: Evidence of climatic and tectonic controls. *Tectonophysics*, 410(1–4), 97–110. Available from: https://doi.org/10.1016/j.tecto.2005.06.010

Törnqvist, T. & Bridge, J.S. (2002) Spatial variation of overbank aggradation rate and its influence on avulsion frequency. *Sedimentology*, 49(5), 891–905. Available from: https://doi.org/10.1046/j.1365-3091.2002.00478.x

Valenza, J.M., Edmonds, D.A., Hwang, T. & Roy, S. (2020) Downstream changes in river avulsion style are related to channel morphology. *Nature Communications*, 11(1), 2116. Available from: https://doi.org/10.1038/s41467-020-15859-9

van Toorenenburg, K.A., Donselaar, M.E., Noordijk, N.A. & Weltje, G.J. (2016) On the origin of crevasse-splay amalgamation in the Huesca river fan (Ebro Basin, Spain): Implications for connectivity in low-net-to-gross river deposits. *Sedimentary Geology*, 343, 156–164. Available from: https://doi.org/10.1016/j.sedgeo.2016.08.008

van Toorenenburg, K.A., Donselaar, M.E. & Weltje, G.J. (2018) The life cycle of crevasse splays as a key mechanism in aggrading dryland rivers. *Earth Surface Processes and Landforms*, 43(11), 2409–2420. Available from: https://doi.org/10.1002/esp.4404

Weissmann, G.S., Hartley, A.J., Nichols, G.J., Scuderi, L.A., Olson, M., Buehler, H. & Banteah, R. (2010) Fluvial form in modern continental sedimentary basins: Distributive fluvial systems. *Geology*, 38(1),

39–42. Available from: https://doi.org/10.1016/j.sedgeo.2012.03.004

Wells, N.A. & Dorr, J.A. (1987) Shifting of the Kosi River, northern India. *Geology*, 15(3), 204–207. Available from: https://doi.org/10.1130/0091-7613(1987)15%3C204:SOTKRN%3E2.0.CO;2

SUPPORTING INFORMATION

Additional supporting information may be found in the online version of the article at the publisher's website.

How to cite this article: Donselaar, M.E., Cuevas Gozalo, M.C., van Toorenenburg, K.A. & Wallinga, J. (2022) Spatio-temporal reconstruction of avulsion history at the terminus of a modern dryland river system. *Earth Surface Processes and Landforms*, 1–17. Available from: https://doi.org/10.1002/esp.5311